Research Square

Preprints are preliminary reports that have not undergone peer review.
They should not be considered conclusive, used to inform clinical practice,
or referenced by the media as validated information.

Model Reference Adaptive Control for Trajectory Tracking and Disturbance Rejection in the Nonlinear Flight Environment Simulation System via Model-Assisted Tracking Extended State Observer

Xiang Xu
Fuzhou University
Feng Huang
Fuzhou University
Xin Wang
Aero Engine Corporation of China
Chao Zhai
China University of Geosciences
Chunyang Zhang
Fuzhou University
Baiyi Zhang
Fuzhou University
Hehong Zhang
HZHANG030@e.ntu.edu.sg

Fuzhou University

Research Article

Keywords:

Posted Date: November 16th, 2026

DOI: https://doi.org/10.21203/rs.3.rs-11493204/v1

License: This work is licensed under a Creative Commons Attribution 4.0 International License.
Read Full License

Additional Declarations: No competing interests reported.

Model Reference Adaptive Control for Trajectory Tracking and Disturbance Rejection in the Nonlinear Flight Environment Simulation System via Model-Assisted Tracking Extended State Observer

Xiang Xu[1,2], Feng Huang[1,2†], Xin Wang[3†], Chao Zhai[4†], Chunyang Zhang[2,5†], Baiyi Zhang[2,5†], Hehong Zhang[2,5*†]

[1]School of Mechanical Engineering and Automation, Fuzhou University, Fuzhou, 350108, Fujian, China.

[2]Advanced Technology Innovation Institute, Fuzhou University, Fuzhou, 350108, Fujian, China.

[3]Sichuan Gas Turbine Research Institute, Aero Engine Corporation of China, Mianyang, 621000, Sichuan, China.

[4]School of Automation, China University of Geosciences, Wuhan, 430074, Hubei, China.

[5*]College of Computer and Data Science Software, Fuzhou University, Fuzhou, 350108, Fujian, China.

*Corresponding author(s). E-mail(s): HZHANG030@e.ntu.edu.sg;
Contributing authors: xiangxu9629@fzu.edu.cn; huangf@fzu.edu.cn;
tywangxin2012@163.com; zhaichao@cug.edu.cn; zhangcy@fzu.edu.cn;
zhangbaiyi@fzu.edu.cn;
†These authors contributed equally to this work.

Abstract

Accurately establishing the intake temperature and pressure conditions in a flight environment simulation system (FESS) is of importance for simulating the actual environment encountered by aeroengines during the flight process. The intake environment simulation system (IESS), however, is a strongly coupled nonlinear plant: the valve flow depends nonlinearly on the opening degree and pressure ratio, the chamber balances involve bilinear state terms, and the thermodynamic coefficients vary with the operating point. These nonlinearities, together with large and fast-varying disturbances, make rapid and precise simulation highly challenging. To address these challenges, a tracking model reference adaptive method integrated with a model-assisted tracking extended state observer (TMRA-MATESO) is proposed. Firstly, the system model is reconstructed by separating the total disturbance into internal and external ones, so that the unmodeled nonlinear dynamics are treated as an internal disturbance rather than being linearized away. Secondly, a model-assisted tracking extended state observer (MATESO) is presented by combining transformed variables with the state-variable parameters, achieving high-precision estimation of external disturbances while reducing the estimation burden

of the extended state observer (ESO). Thirdly, a tracking reference model (TRM) is constructed by improving the conventional reference model (CRM), and an adaptive strategy is designed to adjust the control parameters online against parameter perturbations and internal disturbances. Integrating TMRA with MATESO thus guarantees rapid, accurate tracking under strong nonlinearity and disturbances. The stability of the closed-loop nonlinear system is proved by Lyapunov lemmas and LaSalle's invariance theorem, and extensive experiments demonstrate the superior performance.

Keywords: Nonlinear dynamics, Tracking model reference adaptive (TMRA), Model-assisted tracking extended state observer (MATESO), Disturbance separation mechanism, Intake temperature and pressure control, Flight environment simulation system (FESS)

1 Introduction

As a pivotal ground testing system, the flight environment simulation system (FESS) provides a capability to validate an aeroengine's performance under realistic flight profiles entirely on the ground [1]. As a core subsystem of the FESS, precisely controllable pressure and temperature conditions are provided by the intake environment simulation system (IESS) at the aeroengine intake to construct high-fidelity flight environment test scenarios, thereby enabling the safe operating boundaries of the aeroengine to be accurately obtained [2, 3].

In general, flight environment simulation tasks for aeroengines can be categorized into three types: steady-state environment simulation, transient environment simulation, and continuous flight trajectory environment simulation [4]. Specifically, steady-state environment simulation characterizes operating conditions where flight state parameters (such as altitude, mach number, and aeroengine intake temperature and pressure) remain constant or fluctuate slightly within an allowable threshold; transient environment simulation aims to replicate the working environment of the aeroengine under typical transient states (such as thrust transients, in-flight start/restart), within the boundaries of constant flight altitude and mach number; continuous flight trajectory simulation is dedicated to reproducing the entire flight envelope, encompassing phases such as ground taxiing, accelerated ascent, cruise, and decelerated landing. Currently, control technology for steady-state environment simulation has reached maturity. However, significant challenges remain in the control research on transient and continuous flight trajectory environment simulation [5, 6]. These challenges are mainly attributed to the strong disturbances caused by drastic fluctuations in the aeroengine air mass flow rate (with a rate of change reaching up to 15 kg/s), as well as the difficulties in achieving real-time precise tracking and preventing control failure induced by rapid changes in flight commands (where temperature and pressure change at rates of 1.2 °C/s and 2 kPa/s, respectively). Furthermore, the inevitable presence of other forms of disturbances and model uncertainties in the IESS further exacerbate the control difficulty.

Active disturbance rejection control (ADRC), proposed by Han [7], offers significant engineering practicality with low model dependency and powerful disturbance rejection capabilities. At its core, the method utilizes an extended state observer (ESO) to lump all uncertainties affecting the controlled system into a total disturbance, which is then subjected to real-time estimation and dynamic compensation. Admittedly, ADRC has garnered significant attention due to its superior control performance; however, in practical engineering deployment, the complex parameter tuning process remains a major bottleneck restricting the widespread application. In response, Gao et al. [8] proposed the bandwidth parameterization method, which simplifies the numerous tunable parameters into two core metrics, controller bandwidth and observer bandwidth, thereby significantly reducing the difficulty of algorithm implementation. Since then, ADRC has been widely applied in various fields, such as robotic system [9–11], power system [12–14], vehicle system [15–17], and aerospace system [18–20]. Likewise, ADRC has been widely applied in the IESS [21–23]. Although the aforementioned applications have

achieved satisfactory control performance, simplifying the IESS into a constant-temperature pressure control system severely restricts its applicability in practical complex system. To address this limitation, an ESO-MPC and differential flatness-based multivariable controller was proposed in [24]. Although this approach successfully achieved synchronized control of temperature and pressure, its system response speed remained insufficient for practical engineering applications. To overcome this challenge, Li et al. [25] designed a predefined-time control method, which significantly enhanced the dynamic response speed while maintaining tracking accuracy. Overall, the satisfactory performance achieved by existing control strategies in terms of temperature-pressure regulation accuracy and response speed, several significant disadvantages remain: 1) system model uncertainties (state variables parameters perturbation of system), internal disturbances (control gain deviations), and external disturbances (inter-loop crosstalk and rapid flow fluctuations induced by aeroengine thrust transients) are lumped together as total disturbances, an oversimplified treatment that inevitably imposes an estimation burden and has an adverse effect on the dynamic response of the system; 2) the design of the ESO fails to analyze the characteristics and composition of the target tracking signals (disturbances), resulting in no guarantee of disturbance estimation accuracy; 3) the adoption of an independent design principle (designing the ESO first and then designing the controller under the assumption of perfectly accurate state estimation) neglects the impact of estimation errors on closed-loop system performance, inevitably making it difficult to strictly meet the tracking accuracy requirements.

To solve the aforementioned problems, Jin et al. [26] proposed an MRA-TESO-based method for active magnetic compensation system. While observer estimation performance was improved by this strategy, notable deficiencies remained in terms of dynamic response speed and transient setpoint signals tracking. Therefore, a TMRA-MATESO-based control method is proposed. In brief, the key advantages of the proposed method can be summarized as:

(1) Considering the complex disturbances subject to the IESS, these disturbances are analyzed and separated into internal and external components, thereby reconstructing the mathematical model to effectively reduce the difficulty of disturbance rejection.

(2) By integrating system state variables parameters with transformed variables, MATESO is proposed. This design not only enhances the estimation accuracy of external disturbances but also significantly reduces the estimation burden of the observer.

(3) To overcome the limitation of the CRM in tracking only steady-state inputs, the TRM is proposed to maintain steady-state tracking while achieving precise following of transient inputs, thereby supporting the test requirements for the full flight envelope of aeroengines. Meanwhile, an adaptive mechanism is introduced to reject internal disturbances and parameter perturbations.

(4) Unlike existing independent designs, a coupling mechanism is established between the MATESO and the TMRA. In this framework, the MATESO provides estimates of the system state variables to the TMRA, while the TMRA provides the more accurate IESS model information as feedback to the MATESO. The 'observation-control' synergy enhances control performance, as confirmed by extensive experiments.

The structure of the remainder of this paper is arranged as follows. In section 2, a detailed analysis of the IESS model is presented and its state-space expression is reconstructed through the separation of internal and external disturbances, followed by an elaboration on the control objectives and implementation process of the proposed method. Section 3 details the design of the proposed method for the IESS. In section 4, the stability of the closed-loop control system is rigorously analyzed by using Lyapunov's lemmas and LaSalle's invariance theorem. In section 5, the proposed method is compared with two typical methods based on the experimental platform. Section 6 summarizes the research work of this paper and points out directions for further exploration.

2 State-Space Representation of the IESS Model and Control Objectives

2.1 Model Analysis and State-Space Establishment for the IESS

In this section, the control framework of the IESS is analyzed in detail, and the mathematical descriptions of the critical components are presented in the first part. Then, based on the aforementioned information, the state-space representation of the system is derived.

► Model Analysis

As an integrated control system, the IESS comprises multiple components, which are illustrated in the Fig. 1. These components include the host computer, the PLC, the valves (valve 1 and valve 2), the pipe chambers, the mixing chamber, the sensors, and the flight test chamber [27].

In the IESS, design signals from the host computer and real-time feedback signals acquired by sensors from the mixing chamber are processed by the PLC to generate valve opening commands. Subsequently, valve 1 and valve 2 are actuated by the generated commands, thereby regulating the flow rates of hot stream and cold stream air entering the mixing chamber. Ultimately, the automatic control of the intake environmental pressure and temperature of the aeroengine is achieved.

Based on the analysis of the IESS control framework and workflow, the valve (actuator), the chamber (air mixing and transfer device), and the aeroengine (the object being tested) are being identified as the critical components. Consequently, the focus is being placed on the construction and analysis of the physical models for the aforementioned three components. (1) Valve Model

For the IESS, the butterfly valves shown in Fig. 2 (a) are adopted for both intake loops, with its model comprising motion and air flow characteristic components. The motion characteristic model of valve 1 and valve 2 can be described

$$G_1(s) = \frac{k_{\theta 1}}{t_{\theta 1}s + 1},\ G_2(s) = \frac{k_{\theta 2}}{t_{\theta 2}s + 1}. \tag{1}$$

where $k_{\theta 1} = k_{\theta 2}$ and $t_{\theta 1} = t_{\theta 2}$ denote scale factor and time constant, respectively.

Then, the air flow characteristic model can be expressed as

$$\begin{aligned} W_{in1} &= \varphi S\sqrt{2\rho_1 p_1 \theta_1}, \\ W_{in2} &= \varphi S\sqrt{2\rho_2 p_2 \theta_2}. \end{aligned} \tag{2}$$

where W_{in1}, W_{in2}, S, ρ_1, ρ_2, p_1, p_2, θ_1, and θ_2 are the flow mass rate of hot stream, the flow mass rate of cold stream, the total air flow area of valve, the air density of hot stream, the air density of cold stream, the front-end pressure of valve 1, the front-end pressure of valve 2, the actual opening degree of valve 1, and the actual opening degree of valve 2, respectively. Notably, φ is defined as the air mass flow rate coefficient of valve shown in Fig. 2 (b), which is a function of valve opening degree and pressure ratio across the valve. (2) Chamber Model

Consisting of the pipeline chamber, mixing chamber, and front chamber, the IESS chamber system is simplified into a "two-intake, one-exhaust" model as shown in Fig. 3. Specifically, independent valves regulate the two intake loops, while the exhaust loop supplies the aeroengine under test with the necessary conditions. The following mathematical expression can be derived as the chamber model [28].

$$\begin{aligned} \frac{dT}{dt} &= \frac{RT}{pV(C_P - R)}\Big[(W_{in1} + W_{in2} - W_{out}) \\ &\quad \cdot (RT - h_{out}) + (h_{in1} + \frac{C_{in1}^2}{2})W_{in1} \\ &\quad + (h_{in2} + \frac{C_{in2}^2}{2})W_{in2} \\ &\quad - (h_{out} + \frac{C_{out}^2}{2})W_{out} + \dot{Q}\Big] \\ \frac{dp}{dt} &= \frac{R}{V}\Big[(T - \frac{h_{out} - RT}{C_P - R})(W_{in1} + W_{in2} - W_{out})\Big] \\ &\quad + \frac{R}{V(C_P - R)}\Big[(h_{in1} + \frac{C_{in1}^2}{2})W_{in1} \\ &\quad + (h_{in2} + \frac{C_{in2}^2}{2})W_{in2} \\ &\quad - (h_{out} + \frac{C_{out}^2}{2})W_{out} + \dot{Q}\Big] \end{aligned} \tag{3}$$

(3) Aeroengine Air Flow Characteristic Model

Based on experimental data identification and the analysis process of the chamber model, the

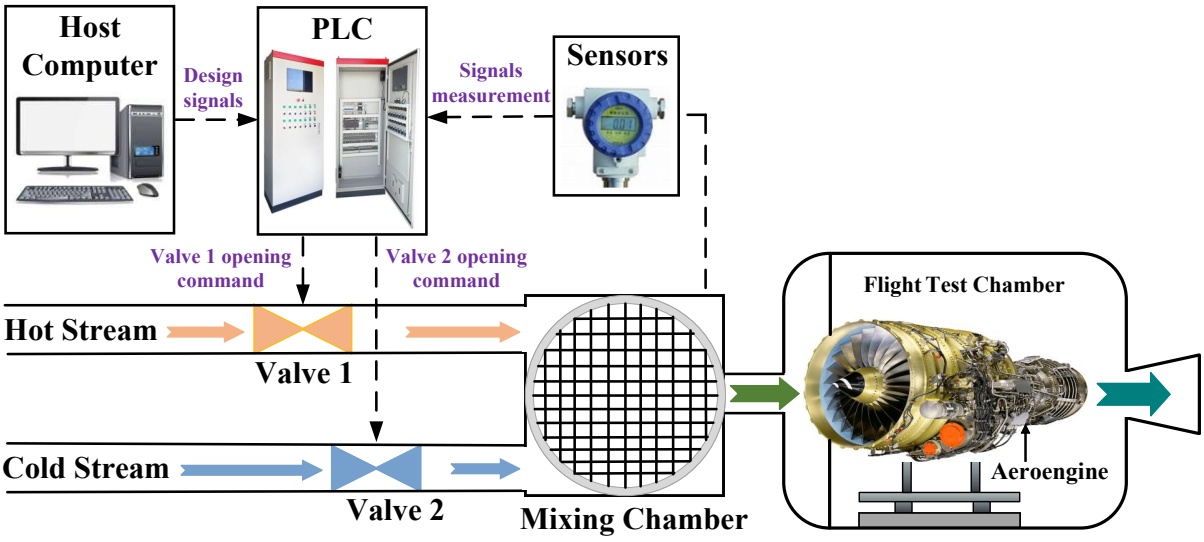
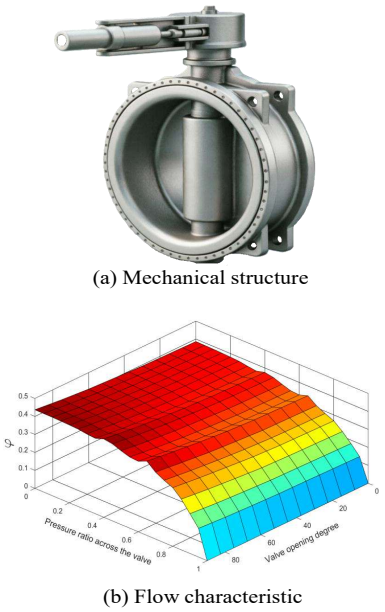


Fig. 1 Control framework of the nonlinear IESS



(a) Mechanical structure

(b) Flow characteristic

Fig. 2 Butterfly valve

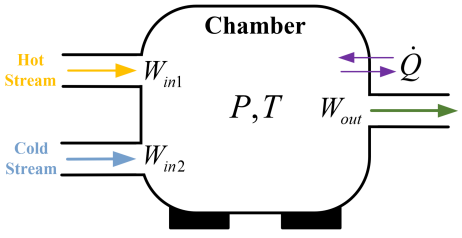


Fig. 3 Simplified chamber model

specific form of the aeroengine air flow characteristic model

$$\begin{cases} W_{out} = W_{aeroengine} = \dfrac{p\sqrt{288.15 \times 15}}{101325\sqrt{T}} W_{ahs}(n_{cl}) \\ n_{cl} = f(H, Ma, n) \end{cases} \tag{4}$$

where W_{ahs}-conversion function of air mass flow rate of aeroengine; n_{cl}-conversion function of fan speed of aeroengine; H-flight altitude; Ma-flight velocity; n-fan speed of aeroengine.

It is worth noting that the specific parameters of the model are provided in Table 1. ▶ State-Space Representation and Model Reconstruction

By combining Eqs.(1-4), the state-space form of the IESS model is given by

$$\begin{cases} \dot{X} = AX + B_0 U_{Tp} + D_f F \\ Y = CX \end{cases} \tag{5}$$

where $X \in R^{4\times1}$, $A \in R^{4\times4}$, $B_0 \in R^{4\times2}$, $U_{Tp} \in R^{2\times1}$, $D_f \in R^{4\times2}$, $F \in R^{2\times1}$, $Y \in R^{2\times1}$, and $C \in R^{2\times4}$ are the state variables vector of the IESS, the state transition matrix, the control gain matrix, the actuator-driven signal vector, the disturbances input matrix, the total disturbances vector, the output vector, and the output coefficients matrix, respectively. Furthermore, a detailed explanation of Eq.(5) is provided below. Firstly, the vector X

Table 1 Parameters of the chamber

Parameter	Interpretation	Unit
T	Temperature	K
p	Pressure	Pa
V	Volume	m^3
R	Air constant	$J/(kg \cdot K)$
C_p	Specific heat capacity	$J/(kg \cdot K)$
W_{out}	Air mass flow rate of the exhaust loop	kg/s
h_{in1}	Enthalpy of the hot stream	J/kg
h_{in2}	Enthalpy of the cold stream	J/kg
h_{out}	Air enthalpy of the exhaust loop	J/kg
C_{in1}	Flow velocity of the hot stream	m/s
C_{in2}	Flow velocity of the cold stream	m/s
C_{out}	Air flow velocity of the exhaust loop	m/s
$\dot{Q}$	Heat exchange rate between chamber and external environment	J/s

and U_{Tp} are defined as

$$X = \begin{bmatrix} X_1^T \\ X_2^T \end{bmatrix},\ U_{Tp} = \begin{bmatrix} u_T \\ u_p \end{bmatrix},\ Y = \begin{bmatrix} T \\ p \end{bmatrix}. \quad (6)$$

where $X_1 = [x_{1T}, x_{1p}]^T$ denote the controlled temperature and pressure, while $X_2 = [x_{2T}, x_{2p}]^T$ represent the corresponding time derivatives; u_T and u_p represent the driving signals of valve 1 and valve 2, respectively.

Next, the forms of matrices A, B_0, D_f, and C are

$$A = \begin{bmatrix} 0 & 0 & 1 & 0 \\ 0 & 0 & 0 & 1 \\ -a_{1T} & 0 & -a_{2T} & 0 \\ 0 & -a_{1p} & 0 & -a_{2p} \end{bmatrix},\ B_0 = \begin{bmatrix} 0 & 0 \\ 0 & 0 \\ b_{0T} & 0 \\ 0 & b_{0p} \end{bmatrix},$$
$$D_f = \begin{bmatrix} 0 & 0 & 1 & 0 \\ 0 & 0 & 0 & 1 \end{bmatrix}^T, C = \begin{bmatrix} 1 & 0 & 0 & 0 \\ 0 & 1 & 0 & 0 \end{bmatrix}.$$

In addition, $F = [f_T, f_p]^T$, where f_T and f_p represent the total disturbances of the temperature and pressure control loops, respectively. To facilitate the subsequent research on the proposed control method, a detailed analysis of F is conducted in what follows. First, the following equation holds

$$f_T = f_{TI} + f_{TE},\ f_p = f_{pI} + f_{pE}. \quad (7)$$

where f_{TI}-internal disturbances in the temperature control loop; f_{TE}-external disturbances in the temperature control loop; f_{pI}-internal disturbances in the pressure control loop; f_{pE}-external disturbances in the pressure control loop.

Furthermore, the expressions for f_{TI}, f_{TE}, f_{pI}, and f_{pE} are shown as

$$\begin{aligned} f_{TI} &= (b_T - b_{0T})u_T, \\ f_{TE} &= \omega_{TE1}(p, \dot{p}) + \omega_{TE2}(\Delta W_{out}). \\ f_{pI} &= (b_p - b_{0p})u_p, \\ f_{pE} &= \omega_{pE1}(T, \dot{T}) + \omega_{pE2}(\Delta W_{out}). \end{aligned} \quad (8)$$

where b_T and b_p denote actual control gain values of the IESS; ω_{TE1} and ω_{pE1} are functions of the inter-loop crosstalk; ω_{TE2} and ω_{pE2} are functions of the air mass flow rate fluctuations of the exhaust loop caused by aeroengine transient environment simulation.

Finally, substituting Eq.(7) into Eq.(5), the system model of the IESS can be reformulated

$$\begin{cases} \dot{X} = AX + B_0 U_{Tp} + D_f(F_I + F_E) \\ Y = CX \end{cases} \quad (9)$$

where $F_I = [f_{TI}, f_{pI}]^T$, $F_E = [f_{TE}, f_{pE}]^T$.

Remark 1. The IESS model in Eq.(9) is nonlinear. Its nonlinearities originate from three sources: (i) the square-root flow–pressure characteristics of the valves in Eq.(2); (ii) the bilinear products of flow rate, enthalpy, and pressure in the chamber balances in Eq.(3); and (iii) the coefficients a_{1T}, a_{2T}, a_{1p}, a_{2p}, b_T, and b_p, which vary with the operating point along the flight envelope.

2.2 Control Objective and Realization Statement

► Control Objective

The control objective of this paper is to enable the environmental conditions (temperature and pressure) at the intake of the aeroengine provided by the IESS to rapidly and accurately track required environmental simulation condition, even in the case of complex disturbances described by Eqs.(7-8). To realize this target, we propose a TMRA-MATESO-based method as shown in Fig. 4 (the descriptions of the variables are given in Table 2), which is translated into the following expression to facilitate the design and analysis of the control method.

$$\lim_{t\to\infty} Y(t) = \Phi_{s1} \tag{10}$$

► Realization Statement

The following step-by-step procedure is developed to realize the control objective in Eq.(10). The details are as follows:

Step 1 A MATESO is designed to achieve accurate estimation of both the system state variables parameters and external disturbances, which can be formulated

$$\lim_{t\to\infty} Z_1(t) = Y,\ \lim_{t\to\infty} Z_2(t) = \dot{Y},\ \lim_{t\to\infty} Z_3(t) = F_E. \tag{11}$$

Step 2 A TRM is presented to ensure unbiased tracking between the reference model's inputs and outputs, expressed as

$$\lim_{t\to\infty} Y_r(t) = \Phi_{s1} \tag{12}$$

Step 3 An adaptive mechanism is introduced to adjust controller parameters in real time, dynamically accommodating system model variations and internal disturbances, thereby driving the IESS model to match the reference model established in ***Step 2***. That is

$$\lim_{t\to\infty} Y(t) = Y_r \tag{13}$$

Step 4 Combining the analysis results of Eqs.(11-13), the proposed method can be constructed, thereby deriving the final expression shown in Eq.(10).

3 Controller Design

The controller based on the TMRA-MATESO mentioned in this section serves to achieve excellent tracking of the required environmental simulation conditions for the IESS and to effectively reject total disturbances.

3.1 Construction of MATESO

As a critical feedback component, MATESO is designed to estimate the system state variables, the corresponding differential signals, and external disturbances in real time, thus fulfilling the objective defined in ***Step 1***.

Firstly, expand the vector F_E in Eq.(9) into the new state vector X_3, and then it can be transformed into

$$\begin{cases} \dot{X}_e = A_e X_e + B_{0e} U_{Tp} + D_{fe} F_I + \dot{G}_E \\ Y = C_e X_e \end{cases} \tag{14}$$

with

$$X_e = \begin{bmatrix} X_1^T & X_2^T & X_3^T \end{bmatrix}^T,\ X_3 = \begin{bmatrix} x_{3T} & x_{3p} \end{bmatrix}^T,$$

$$A_e = \begin{bmatrix} 0 & 0 & 1 & 0 & 0 & 0 \\ 0 & 0 & 0 & 1 & 0 & 0 \\ -a_{1T} & 0 & -a_{2T} & 0 & 1 & 0 \\ 0 & -a_{1p} & 0 & -a_{2p} & 0 & 1 \\ 0 & 0 & 0 & 0 & 0 & 0 \\ 0 & 0 & 0 & 0 & 0 & 0 \end{bmatrix},$$

$$B_{0e} = \begin{bmatrix} 0 & 0 \\ 0 & 0 \\ b_{0T} & 0 \\ 0 & b_{0p} \\ 0 & 0 \\ 0 & 0 \end{bmatrix},\ D_{fe} = \begin{bmatrix} 0 & 0 \\ 0 & 0 \\ 1 & 0 \\ 0 & 1 \\ 0 & 0 \\ 0 & 0 \end{bmatrix}, \dot{G}_E = \begin{bmatrix} 0 \\ 0 \\ 0 \\ 0 \\ \dot{g}_{TE} \\ \dot{g}_{pE} \end{bmatrix},$$

$$C_e = \begin{bmatrix} 1 & 0 & 0 & 0 & 0 & 0 \\ 0 & 1 & 0 & 0 & 0 & 0 \end{bmatrix}.$$

Next, according to Eq.(14), the transformed observer is formulated by introducing transformation variables as

$$\begin{aligned} \dot{Z}_{M,Tran} = {} & (A_e - L_M C_e) Z_{M,Tran} \\ & + B_{0e} U_{Tp} + D_{fe} F_I + L_M Y \end{aligned} \tag{15}$$

where the estimated vector $Z_{M,Tran} = [Z_{M1}^T, Z_{M2}^T, Z_{M3,Tran}^T]^T$, and its internal elements are: $Z_{M1} = [z_{m1T}, z_{m1p}]^T$, $Z_{M2} = [z_{m2T}, z_{m2p}]^T$,

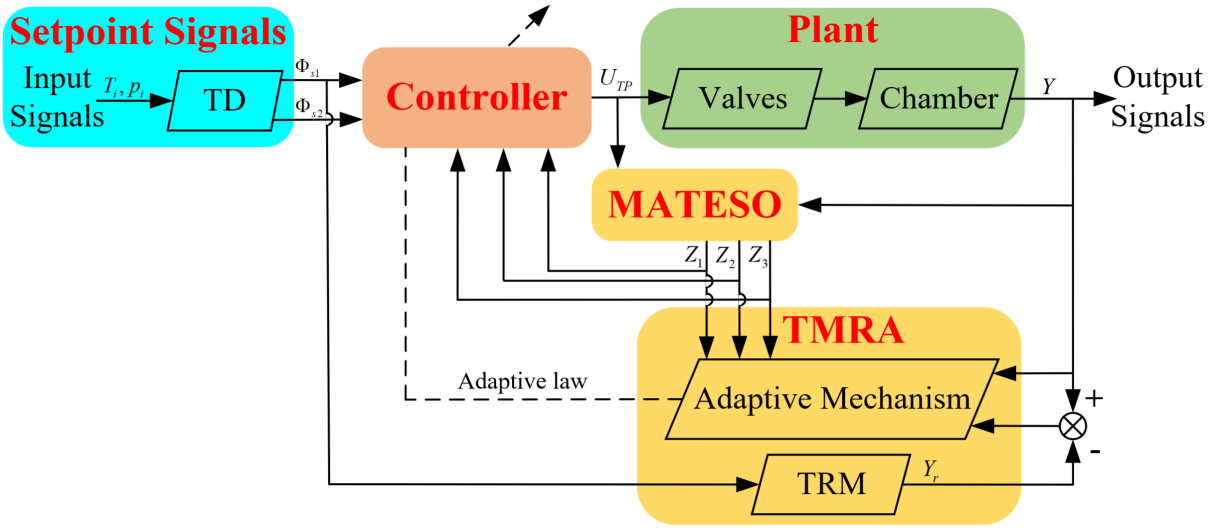


Fig. 4 The overall block diagram of the TMRA-MATESO-based method

Table 2 Variables of the Fig. 4

Variable	Construction	Interpretation
T_i	—	Input temperature
p_i	—	Input pressure
Φ_{s1}	$[T_s, p_s]^T$	Setpoint signals
Φ_{s2}	$[\dot{T}_s, \dot{p}_s]^T$	Differentiation of Φ_{s1}
Z_1	$[z_{1T}, z_{1p}]^T$	Estimates of temperature and pressure
Z_2	$[z_{2T}, z_{2p}]^T$	Differentiation of Z_1
Z_3	$[z_{3T}, z_{3p}]^T$	Estimates of external disturbances
Y_r	$[T_r, p_r]^T$	Temperature and pressure output by the TRM

and $Z_{M3,Tran} = [z_{m3T,Tran}, z_{m3p,Tran}]^T$; the gain matrix $L_M = [L_{M1}, L_{M2}, L_{M3}]^T$, and its internal elements are: $L_{M1} = \text{diag}\{l_{m1T}, l_{m1p}\}$, $L_{M2} = \text{diag}\{l_{m2T}, l_{m2p}\}$, and $L_{M3} = \text{diag}\{l_{m3T}, l_{m3p}\}$. At the same time, $l_{m1T}, l_{m1p}, l_{m2T}, l_{m2p}, l_{m3T}, l_{m3p} \in R^+$.

From Eq.(15), $Z_{M3,Tran}$ is given by

$$Z_{M3,Tran} = \Upsilon Z_{M3} \tag{16}$$

where $\Upsilon = \text{diag}\{\frac{\omega_T^2}{s^2+2\xi_T\omega_T s+\omega_T^2}, \frac{\omega_p^2}{s^2+2\xi_p\omega_p s+\omega_p^2}\}$ with $\xi_T = \frac{a_{1T}+l_{m2T}}{2l_{m3T}}\sqrt{\frac{l_{m3T}}{a_{2T}}}$, $\xi_p = \frac{a_{1p}+l_{m2p}}{2l_{m3p}}\sqrt{\frac{l_{m3p}}{a_{2p}}}$, $\omega_T = \sqrt{\frac{l_{m3T}}{a_{2T}}}$, and $\omega_p = \sqrt{\frac{l_{m3p}}{a_{2p}}}$; $Z_{M3} = [z_{m3T}, z_{m3p}]^T$ represents the external disturbances estimation vector of the MATESO.

Then, the observation error vector of the MATESO is formulated

$$E_M = X_e - Z_M = \left[E_{M1}^T \; E_{M2}^T \; E_{M3}^T\right]^T \tag{17}$$

where $Z_M = [Z_{M1}^T, Z_{M2}^T, Z_{M3}^T]^T$; $E_{M1} = [x_{1T} - z_{m1T}, x_{1p} - z_{m1p}]^T$, $E_{M2} = [x_{2T} - z_{m2T}, x_{2p} - z_{m2p}]^T$, $E_{M3} = [x_{3T} - z_{m3T}, x_{3p} - z_{m3p}]^T$.

Based on Eqs.(15-17), the structure of the MATESO can be described

$$\dot{Z}_M = \Gamma Z_M + B_{0e}U_{Tp} + D_{fe}F_I + L_{M1}Y_M + \Pi\dot{E}_{M2} \tag{18}$$

with

$$Y_M = [Y^T \; \dot{Y}^T],$$

$$\Gamma = \begin{bmatrix} -l_{m1T} & 0 & 1 & 0 & 0 & 0 \\ 0 & -l_{m1p} & 0 & 1 & 0 & 0 \\ 0 & 0 & 0 & 0 & 1 & 0 \\ 0 & 0 & 0 & 0 & 0 & 1 \\ -l_{m3T} & 0 & -(a_{1T}+l_{m2T}) & 0 & 0 & 0 \\ 0 & -l_{m3p} & 0 & -(a_{1p}+l_{m2p}) & 0 & 0 \end{bmatrix},$$

$$L_{M1} = \begin{bmatrix} l_{m1T} & 0 & 0 & 0 \\ 0 & l_{m1p} & 0 & 0 \\ -a_{1T} & 0 & -a_{2T} & 0 \\ 0 & -a_{1p} & 0 & -a_{2p} \\ l_{m3T} & 0 & (a_{1T}+l_{m2T}) & 0 \\ 0 & l_{m3p} & 0 & (a_{1p}+l_{m2p}) \end{bmatrix},$$

$$\Pi = \begin{bmatrix} 0 & 0 & 0 & 0 & a_{2T} & 0 \\ 0 & 0 & 0 & 0 & 0 & a_{2p} \end{bmatrix}^T.$$

It is worth noting that the internal disturbances (F_I) and system dynamic parameters (a_{1T}, a_{1p}, a_{2T}, and a_{2p}) in Eq.(18) will be provided by the subsequent adaptive mechanism in ***Step 3***, which is designed to make the IESS model approximate the TRM proposed in ***Step 2***. This integration forms a unified control framework across ***Step 1*** to ***Step 3***, effectively enhancing the overall control performance of the system.

Thereafter, by subtracting Eq.(18) from Eq.(14) and substituting Eq.(17), we obtain

$$\dot{E}_M = \Gamma E_M - \Pi \dot{E}_{M2} + \dot{G}_E \tag{19}$$

By performing certain mathematical operations on Eq.(19), the following conclusion can be drawn

$$\begin{cases} E_{M1}(s) = \left(Is^2 + L_{M1}s\right)^{-1} E_{M3}(s) \\ E_{M3}(s) = \Psi_M(s) G_{E1}(s) \end{cases} \tag{20}$$

with

$$\Psi_M(s) = \mathrm{diag}\left\{ \frac{s^3 + l_{m1T}s^2}{s^3 + (a_{2T}+l_{m1T})s^2 + (a_{1T}+l_{m2T})s + l_{m3T}}, \right.$$
$$\left. \frac{s^3 + l_{m1p}s^2}{s^3 + (a_{2p}+l_{m1p})s^2 + (a_{1p}+l_{m2p})s + l_{m3p}} \right\},$$

$$G_{E1}(s) = [\, g_{TE}(s),\ g_{pE}(s)\,]^T.$$

By examining the mathematical form of Eq.(20), the conclusion can be obtained: $\lim_{t\to\infty} E_{M1}(t) = 0$ and $\lim_{t\to\infty} E_{M2}(t) = 0$ are achieved only when $\lim_{t\to\infty} E_{M3}(t) = 0$. Therefore, the problem is transformed into the precise tracking of external disturbances.

Although the specific mathematical expression of the external disturbances described in Eq.(8) is unknown, partial information can still be obtained through its structural characteristics. Specifically, the inter-loop crosstalk (ω_{TE1} and ω_{pE1}) can generally be regarded as noise of electrical and approximated using an impulse function [29]; meanwhile, the drastic fluctuations in aero-engine air mass flow rate (ω_{TE2} and ω_{pE2}) typically exhibit a curve composed of approximately constant and ramp functions [2, 21, 24, 25].

Based on the above, the following linear combination expression vector can be selected to verify the estimation capability of MATESO for the two forms of external disturbances

$$\begin{aligned} G_{E1}(t) &= \left[g_{TE}(t)\ \ g_{pE}(t)\right]^T \\ &= \begin{bmatrix} k_{1T}\delta_T + k_{2T} + k_{3T}t \\ k_{1p}\delta_p + k_{2p} + k_{3p}t \end{bmatrix} \end{aligned} \tag{21}$$

where $k_{1T}, k_{2T}, k_{3T}, k_{1p}, k_{2p}, k_{3p} \in \mathbb{R}$.

Taking the Laplace transform of Eq.(21) yields

$$G_{E1}(s) = \left[k_{1T} + \frac{k_{2T}}{s} + \frac{k_{3T}}{s^2}\ \ k_{1p} + \frac{k_{2p}}{s} + \frac{k_{3p}}{s^2}\right]^T \tag{22}$$

By combining Eqs.(20) and (22) and applying the final value theorem, the result is achieved

$$\lim_{t\to\infty} E_{M3}(t) = \lim_{s\to 0} sE_{M3}(s) = 0 \tag{23}$$

On the basis of Eq.(23), it can be further derived that

$$\lim_{t\to\infty} E_{M1}(t) = 0,\ \lim_{t\to\infty} E_{M2}(t) = 0. \tag{24}$$

Combining with Eqs.(23-24) can get

$$\begin{aligned} &\lim_{t\to\infty} Z_{M1}(t) = Y,\ \lim_{t\to\infty} Z_{M2}(t) = \dot{Y}, \\ &\lim_{t\to\infty} Z_{M3}(t) = F_E. \end{aligned} \tag{25}$$

3.2 Architecture of TRM from CRM

The form of the reference model not only determines the realizability of ***Step 2***, but also serves as a prerequisite for the implementation of the proposed method.

▶ Characterization of CRM

The CRM is typically expressed as

$$\begin{cases} \dot{X}_{Cr} = A_r X_{Cr} + B_r \Phi_{s1} \\ Y_{Cr} = C_r X_{Cr} \end{cases} \tag{26}$$

where $X_{Cr} = [X_{Cr1}^T, X_{Cr2}^T]^T$ is the state variable vector, and the detail information as: $X_{Cr1} = [x_{cr-1Tr}, x_{cr-1pr}]^T$, $X_{Cr2} = [x_{cr-2Tr}, x_{cr-2pr}]^T$.

Furthermore, the A_r, B_r, and C_r are

$$A_r = \begin{bmatrix} 0 & 0 & 1 & 0 \\ 0 & 0 & 0 & 1 \\ -a_{1Tr} & 0 & -a_{2Tr} & 0 \\ 0 & -a_{1pr} & 0 & -a_{2pr} \end{bmatrix},$$
$$B_r = \begin{bmatrix} 0 & 0 & b_{1Tr} & 0 \\ 0 & 0 & 0 & b_{1pr} \end{bmatrix}^T, C_r = \begin{bmatrix} 1 & 0 & 0 & 0 \\ 0 & 1 & 0 & 0 \end{bmatrix}.$$

where $a_{1Tr}, a_{2Tr}, a_{1pr}, a_{2pr}, b_{1Tr}, b_{1pr} \in R^+$, with $a_{1Tr} = b_{1Tr}$ and $a_{1pr} = b_{1pr}$.

Next, the tracking performance of the CRM described by Eq.(26) is analyzed. Obviously, the unit open-loop transfer function from input Φ_{s1} to output Y_{Cr} is

$$\begin{aligned} G_C(s) &= \begin{bmatrix} G_{TC}(s) & G_{pC}(s) \end{bmatrix}^T \\ &= \begin{bmatrix} \frac{b_{1Tr}}{s(s+a_{2Tr})} & \frac{b_{1pr}}{s(s+a_{2pr})} \end{bmatrix}^T \end{aligned} \tag{27}$$

Analogous to the analytical framework of the MATESO performance evaluation, we proceed to analyze the setpoint signals of the IESS system. As the signals contain steady-state and transient components, the following linear combination expression vector is adopted to validate the tracking performance of CRM for the setpoint signals

$$\Phi_{s1}(t) = \begin{bmatrix} k_{4T} + k_{5T}t & k_{4p} + k_{5p}t \end{bmatrix}^T \tag{28}$$

where $k_{4T}, k_{5T}, k_{4p}, k_{5p} \in \mathbb{R}$, and these coefficients are treated as variable.

Taking the Laplace transform of Eq.(28) and incorporating Eq.(27), followed by the application of the final value theorem, leads to the expression

$$\begin{aligned} &\lim_{t\to\infty} E_{ssc}(t) \\ &= \lim_{s\to 0} s\big(I + \mathrm{diag}\{G_{TC}(s), G_{pC}(s)\}\big)^{-1}\Phi_{s1}(s) \\ &= \begin{bmatrix} \frac{a_{2Tr}k_{5T}}{b_{1Tr}} & \frac{a_{2pr}k_{5p}}{b_{1pr}} \end{bmatrix}^T \neq 0 \end{aligned} \tag{29}$$

Further, Eq.(29) can be elaborated

$$\lim_{t\to\infty} Y_{Cr}(t) \neq \Phi_{s1} \tag{30}$$

► Description of TRM

It is clear from Eq.(30) that the CRM cannot meet the condition shown in Eq.(12). To solve this problem, the TRM is proposed, which is described

$$\begin{cases} \dot{X}_{Tr} = A_r X_{Tr} + B_r \Phi_{s1} + D_r \Phi_{s2} \\ Y_{Tr} = C_r X_{Tr} \end{cases} \tag{31}$$

where $X_{Tr} = [X_{Tr1}^T, X_{Tr2}^T]^T$ is the state variable vector. More detail, $X_{Tr1} = [x_{tr-1Tr}, x_{tr-1pr}]^T$, $X_{Tr2} = [x_{tr-2Tr}, x_{tr-2pr}]^T$. Besides, $D_r = \begin{bmatrix} 0 & 0 & a_{2Tr} & 0 \\ 0 & 0 & 0 & a_{2pr} \end{bmatrix}^T$.

Accordingly, the unit open-loop transfer function with input Φ_{s1} and output Y_{Tr} is modified to

$$\begin{aligned} G_T(s) &= \begin{bmatrix} G_{TT}(s) & G_{pT}(s) \end{bmatrix}^T \\ &= \begin{bmatrix} \frac{a_{2Tr}s+b_{1Tr}}{s^2} & \frac{a_{2pr}s+b_{1pr}}{s^2} \end{bmatrix}^T \end{aligned} \tag{32}$$

Then, the steady-state error can be expressed as

$$\begin{aligned} &\lim_{t\to\infty} E_{sst}(t) \\ &= \lim_{s\to 0} s\big(I + \mathrm{diag}\{G_{TT}(s), G_{pT}(s)\}\big)^{-1}\Phi_{s1}(s) \\ &= 0 \end{aligned} \tag{33}$$

Ultimately, the conclusion can be drawn

$$\lim_{t\to\infty} Y_{Tr}(t) = \Phi_{s1} \tag{34}$$

3.3 Design of Controller

A TMRA-MATESO-based method is adopted to guarantee the realization of ***Step 4***, with its mathematical expression presented below

$$\begin{aligned} U_{Tp} = (B_0^T B_0)^{-1} B_0^T \big(&- \hat{K}_x [Z_{M1}^T, Z_{M2}^T]^T \\ &- D_f(\hat{F}_I + Z_{M3}) + B_r \Phi_{s1} + D_r \Phi_{s2}\big) \end{aligned} \tag{35}$$

where $\hat{K}_x$ and $\hat{F}_I$ represent the estimates of $K_x = A - A_r = \begin{bmatrix} 0 & 0 & 0 & 0 \\ 0 & 0 & 0 & 0 \\ k_{1T} & 0 & k_{2T} & 0 \\ 0 & k_{1p} & 0 & k_{2p} \end{bmatrix}$ and F_I to meet the criteria of ***Step 3***. Such values can be obtained by integrating the expression

$$\dot{\hat{K}}_x = -\Lambda_x P E X^T, \ \dot{\hat{F}}_I = -\Lambda_I D_f^T P^T E. \tag{36}$$

About Eq.(36), E represents the system error, which is defined

$$\begin{aligned} E &= X_{Tr} - X = \left[E_1^T \;\; E_2^T\right]^T. \\ E_1 &= \left[e_{1T} \;\; e_{1p}\right]^T \\ &= \left[x_{tr-1Tr} - x_{1T} \;\; x_{tr-1pr} - x_{1p}\right]^T, \\ E_2 &= \left[e_{2T} \;\; e_{2p}\right]^T \\ &= \left[x_{tr-2Tr} - x_{2T} \;\; x_{tr-2pr} - x_{2p}\right]^T. \end{aligned} \tag{37}$$

Besides, Λ_x, Λ_I, and P of Eq.(36) are given

$$\Lambda_x = \mathrm{diag}\{\lambda_{Tx}, \lambda_{px}, \lambda_{Tx}, \lambda_{px}\},$$
$$\Lambda_I = \mathrm{diag}\{\lambda_{TI}, \lambda_{pI}\},\; P = \begin{bmatrix} p_1 & 0 & p & 0 \\ 0 & p_1 & 0 & p \\ p & 0 & p_2 & 0 \\ 0 & p & 0 & p_2 \end{bmatrix}.$$

where $\lambda_{Tx}, \lambda_{px}, \lambda_{TI}, \lambda_{pI}, p, p_1, p_2 \in R^+$.

4 Stability and Convergence Analysis

Theorem 1: The controller proposed (35) with the update law (36) ensures the IESS provides accurate required environmental simulation conditions (temperature and pressure) at the intake of the aeroengine, namely

$$\lim_{t\to\infty} T(t) = T_s,\; \lim_{t\to\infty} p(t) = p_s. \tag{38}$$

Proof: First, choose Lyapunov function as

$$\begin{aligned} V &= \frac{1}{2}E^T P E \\ &+ \frac{1}{2}\mathrm{tr}(\tilde{K}_x^T \Lambda_x^{-1} \tilde{K}_x) + \frac{1}{2}\tilde{F}_I^T \Lambda_I^{-1} \tilde{F}_I \geq 0 \end{aligned} \tag{39}$$

where $\tilde{K}_x = \hat{K}_x - K_x$ and $\tilde{F}_I = \hat{F}_I - F_I$ are estimation errors. Taking the time derivative of $\tilde{K}_x$ and $\tilde{F}_I$, we have

$$\dot{\tilde{K}}_x = \dot{\hat{K}}_x, \dot{\tilde{F}}_I = \dot{\hat{F}}_I \tag{40}$$

Then, taking the time derivative of Eq.(37) and incorporating Eqs.(9), (31), and (35), the result can be obtained

$$\begin{aligned} \dot{E} &= \dot{X}_{Tr} - \dot{X} \\ &= A_r X_{Tr} + B_r \Phi_{s1} + D_r \Phi_{s2} \\ &- AX - B_0 U_{Tp} - D_f(F_I + F_E) \\ &= A_r X_{Tr} - AX + \hat{K}_x [Z_{M1}^T, Z_{M2}^T]^T \\ &+ D_f(\hat{F}_I + Z_{M3}) - D_f(F_I + F_E) \end{aligned} \tag{41}$$

Combining Eqs.(9), (25) and (37), Eq.(41) can be further written as

$$\begin{aligned} \dot{E} &= A_r X_{Tr} + (\hat{K}_x - A)X + D_f(\hat{F}_I - F_I) \\ &= A_r X_{Tr} + (\tilde{K}_x + K_x - A)X + D_f \tilde{F}_I \\ &= A_r X_{Tr} - A_r X + \tilde{K}_x X + D_f \tilde{F}_I \\ &= A_r E + \tilde{K}_x X + D_f \tilde{F}_I \end{aligned} \tag{42}$$

Differentiating V and simplifying based on Eqs.(36), (40) and (42) yields

$$\begin{aligned} \dot{V} &= \frac{1}{2}\dot{E}^T P E + \frac{1}{2}E^T P \dot{E} \\ &+ \mathrm{tr}(\tilde{K}_x^T \Lambda_x^{-1} \dot{\tilde{K}}_x) + \tilde{F}_I^T \Lambda_I^{-1} \dot{\tilde{F}}_I \\ &= \frac{1}{2}E^T A_r^T P E + \frac{1}{2}E^T P A_r E \\ &+ E^T P(\tilde{K}_x X + D_f \tilde{F}_I) \\ &+ \mathrm{tr}(\tilde{K}_x^T \Lambda_x^{-1} \dot{\tilde{K}}_x) + \tilde{F}_I^T \Lambda_I^{-1} \dot{\tilde{F}}_I \\ &= \frac{1}{2}E^T (A_r^T P + P A_r) E \\ &+ \mathrm{tr}\big(\tilde{K}_x^T (P E X^T + \Lambda_x^{-1} \dot{\tilde{K}}_x)\big) \\ &+ \tilde{F}_I^T (D_f^T P^T E + \Lambda_I^{-1} \dot{\tilde{F}}_I) \\ &= -E^T Q E + \mathrm{tr}\big(\tilde{K}_x^T (P E X^T + \Lambda_x^{-1} \dot{\hat{K}}_x)\big) \\ &+ \tilde{F}_I^T (D_f^T P^T E + \Lambda_I^{-1} \dot{\hat{F}}) \\ &= -E^T Q E \end{aligned} \tag{43}$$

where $A_r^T P + P A_r = -2Q$, and the detail form of Q is

$$Q = \begin{bmatrix} a_{1Tr}p & 0 & \frac{a_{2Tr}p + a_{1Tr}p_2 - p_1}{2} & 0 \\ 0 & a_{1pr}p & 0 & \frac{a_{2pr}p + a_{1pr}p_2 - p_1}{2} \\ \frac{a_{2Tr}p + a_{1Tr}p_2 - p_1}{2} & 0 & a_{2Tr}p_2 - p & 0 \\ 0 & \frac{a_{2pr}p + a_{1pr}p_2 - p_1}{2} & 0 & a_{2pr}p_2 - p \end{bmatrix}$$

The following rules for parameter selection can be established

$$\begin{cases} p_1 = a_{2Tr}p + a_{1Tr}p_2 = a_{2pr}p + a_{1pr}p_2 \\ a_{2Tr}p_2 > p \\ a_{2pr}p_2 > p \end{cases} \tag{44}$$

Subsequently, we have

$$\dot{V} = -E^T Q E \leq 0 \tag{45}$$

In order to complete the proof, the following invariant and compact set S is introduced

$$S = \left\{ (E, \dot{E}) \mid \dot{V} = 0 \right\} \tag{46}$$

The largest invariance set contained in S is defined as Ω. It can be concluded that in Ω

$$\lim_{t\to\infty} E(t) = 0 \tag{47}$$

Based on Eq.(47), the following result is clearly valid

$$\lim_{t\to\infty} Y(t) = Y_{Tr} \tag{48}$$

Finally, a comprehensive analysis of Eqs.(34) and (48) leads to

$$\lim_{t\to\infty} Y(t) = \Phi_{s1} \Rightarrow \lim_{t\to\infty} T(t) = T_s, \ \lim_{t\to\infty} p(t) = p_s. \tag{49}$$

According to the the above conclusions, the equilibrium point of the closed-loop system is contained within the largest invariant set Ω. Moreover, the proof of ***Theorem 1*** is accomplished through LaSalle's invariance principle [30].

5 Experimental Results and Discussion

In this section, the proposed controller is verified using the experimental platform shown in Fig. 5, which consists of two regulating valves, a hydraulic power drive (HPD), a programmable logic controller (PLC), a host computer (HC), and a human-machine interface (HMI). The control logic is developed in Automation Studio on the HC and deployed to the PLC via Ethernet. During operation, an encoder detects the real-time valve stem position, which is fed back to the PLC to calculate the valve opening. Accordingly, the PLC issues command signals to the servo amplifier, driving the HPD to actuate the valves and regulate the air mass flow rate. To ensure reliability, the assembly incorporates a solenoid directional valve (SDV) as a safety mechanism. Meanwhile, the HMI provides real-time visualization of the system's dynamic response.

A series of experiments and analyses are conducted to verify the performance of the proposed method. Specifically, we will divide the experiment tests into two groups: the first group compares the proposed method with the barrier lyapunov function-based predefined-time disturbance rejection (BLF-PTDR) method [25] and a model design adaptive extended state observer with tracking filter (MRA-TESO) method [26] from Jin's research to evaluate its control performance, including tracking accuracy and response time; the second group to assess the robustness of the proposed method, simulations are conducted under the environmental simulations of transient and continuous flight trajectories, respectively, which specifically encompass its disturbance rejection capability and wide applicability.

5.1 Experimental Conditions

▶ Parameters Configuration of the IESS

The specific values for the IESS parameters are listed below [31].

$$\begin{aligned} &V = 300\,\mathrm{m}^3,\ R = 287\,\mathrm{J/(kg\cdot K)}, \\ &p_1 = 180000\,\mathrm{Pa},\ p_2 = 120000\,\mathrm{Pa}, \\ &\rho_1 = 2.069\,\mathrm{kg/m}^3,\ \rho_2 = 2.283\,\mathrm{kg/m}^3, \\ &k_{\theta 1} = k_{\theta 2} = 1,\ t_{\theta 1} = t_{\theta 2} = 1.4. \end{aligned} \tag{50}$$

▶ Setpoint Signals

The input signals about temperature and pressure can be obtained

$$\begin{cases} T_i(t) = T_H(t)\big(1 + 0.2Ma^2(t)\big) \\ p_i(t) = p_H(t)\big(1 + 0.2Ma^2(t)\big)^{3.5} \end{cases} \tag{51}$$

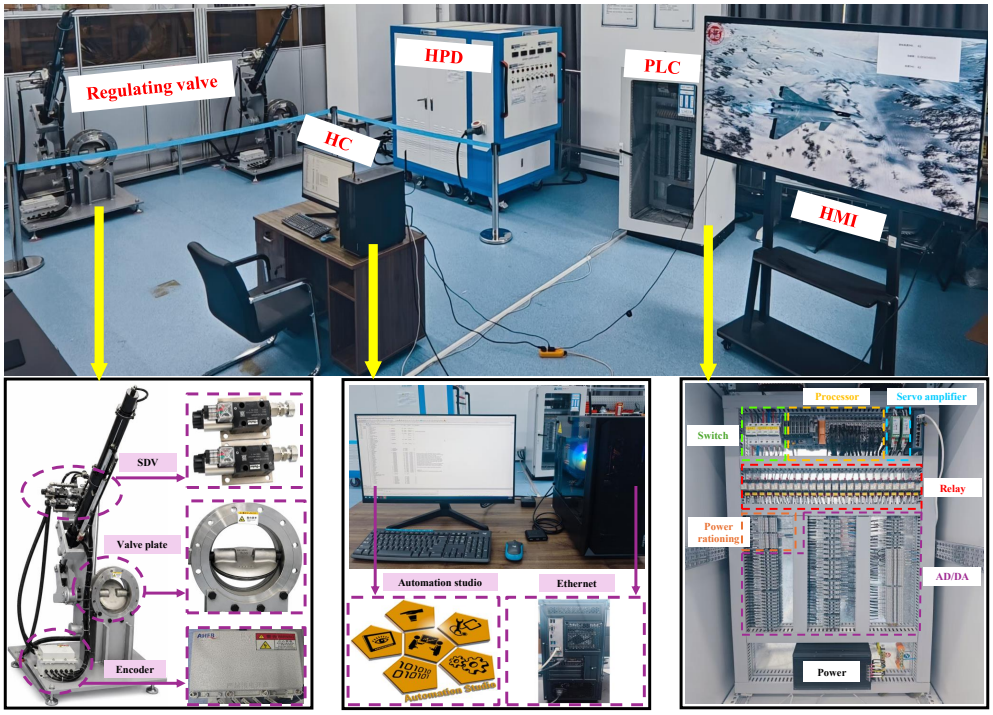


Fig. 5 Experimental platform

where $T_H(t)$ and $p_H(t)$ can be expressed

$$T_H(t) = \begin{cases} T_0 - 6.5H(t), & H \le 11 \\ 216.5, & H > 11 \end{cases},$$

$$p_H(t) = \begin{cases} p_0 \left(1 - \frac{H(t)}{44.3}\right)^{5.255}, & H \le 11 \\ 2.26 \cdot 10^4 \cdot e^{\frac{11 - H(t)}{6.318}}, & H > 11 \end{cases}$$

where $T_0 = 288.15$ K, and $p_0 = 101325$ Pa represent the standard values of temperature and pressure, respectively.

Generally, the tracking differentiator (TD) is frequently utilized in ADRC designs for input signals smoothing and differential signals extraction, thereby generating the design signals. It is mathematically formulated as

$$\Phi_{k+1} = K_h \Phi_k + H_{fst}$$

where define $\Phi_{k+1} = [T_{1s}(k+1), p_{1s}(k+1), T_{2s}(k+1), p_{2s}(k+1)]^T$ and $\Phi_k = [T_{1s}(k), p_{1s}(k), T_{2s}(k), p_{2s}(k)]^T$. Here, Φ_{k+1} and Φ_k represent the vector of state variables at the next moment and the current moment, respectively. In addition, the matrix K_h and H_{fst} are

$$K_h = \begin{bmatrix} 1 & 0 & h_T & 0 \\ 0 & 1 & 0 & h_p \\ 0 & 0 & 1 & 0 \\ 0 & 0 & 0 & 1 \end{bmatrix},$$

$$H_{fst} = \begin{bmatrix} 0 \\ 0 \\ h_T fst(T_{1s} - T_s, T_{2s}, r_T, h_T) \\ h_p fst(p_{1s} - p_s, p_{2s}, r_p, h_p) \end{bmatrix}.$$

with

$$\mathrm{fst}(x_1, x_2, r, h) = \begin{cases} -\frac{ra}{h}, & |a| \le d \\ -r \ \mathrm{sign}(a), & |a| > d \end{cases},$$

$$\begin{cases} d = rh, \quad d_0 = dh \\ y = x_1 + hx_2 \end{cases},$$

$$a = \begin{cases} x_2 + \frac{y}{h}, & |y| \le d_0 \\ x_2 + \frac{1}{2}\left(\sqrt{d^2 + 8r|y|} - rh\right) \mathrm{sign}(y), & |y| > d_0 \end{cases}$$

In particular, the TD parameters are given as

$$h_T = h_p = 0.2, \ r_T = r_p = 6000. \tag{52}$$

5.2 Comparative Experiments

The effectiveness of the proposed method is demonstrated through extensive numerical experiments, which offer a direct performance comparison with BLF-PTDR method and MRA-TESO method.

► Environmental Simulation Task Setup

The environmental simulation task of takeoff process is selected as the setpoint, and the detailed expression are

$$Ma(t)=\begin{cases}0, & 0\le t\le 55\\ \frac{1111}{10000}t-\frac{116655}{10000}, & 55<t\le 100\\ \frac{1}{2}, & t>100\end{cases},$$
$$H(t)=\begin{cases}0, & 0\le t\le 55\\ \frac{11111}{100000}t-\frac{1166655}{10000}, & 55<t\le 100\\ 5, & t>100\end{cases} \tag{53}$$

Based on Eqs.(50-53), Fig. 6 presents the setpoints for the takeoff process environmental simulation task, which are, from top to bottom, flight Mach number, flight altitude, throttle lever angle, aeroengine air mass flow rate, temperature, and pressure. In addition, the task can be divided into three consecutive phases: the ground taxi (yellow region), the accelerated ascent (pink region), and the cruise (cyan region).

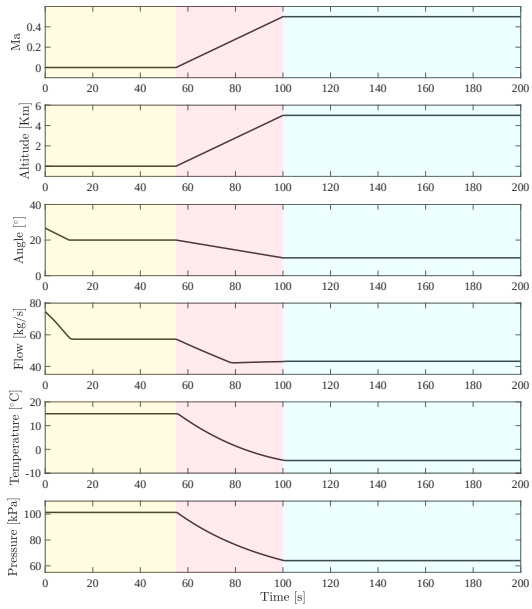


Fig. 6 Setpoints of environmental simulation task for the takeoff process

► Comparison Method

(1) BLF-PTDR Method

The ESO is designed as

$$\dot{Z}_{BP}=(A_{BP}-L_{BP}C_{BP})Z_{BP}+B_{BP}U_{Tp}+L_{BP}Y$$

where $Z_{BP}=[Z_{BP1}^T,Z_{BP2}^T,Z_{BP3}^T]^T$ represents the estimation vector of the state of the system. In detail, $Z_{BP1}=[z_{bp1T},z_{bp1p}]^T$, $Z_{BP2}=[z_{bp2T},z_{bp2p}]^T$, and $Z_{BP3}=[z_{bp3T},z_{bp3p}]^T$. Besides, the A_{BP}, B_{BP}, L_{BP}, and C_{BP} are

$$A_{BP}=\begin{bmatrix}0&0&1&0&0&0\\0&0&0&1&0&0\\0&0&0&0&1&0\\0&0&0&0&0&1\\0&0&0&0&0&0\\0&0&0&0&0&0\end{bmatrix},\ B_{BP}=\begin{bmatrix}0&0\\0&0\\1&0\\0&1\\0&0\\0&0\end{bmatrix},$$
$$L_{BP}=\begin{bmatrix}l_{bp1T}&0\\0&l_{bp1p}\\l_{bp2T}&0\\0&l_{bp2p}\\l_{bp3T}&0\\0&l_{bp3p}\end{bmatrix},C_{BP}=\begin{bmatrix}1&0&0&0&0&0\\0&1&0&0&0&0\end{bmatrix}.$$

The control law can be expressed as

$$U_{BP}=B_{BP}^{-1}\left\{\dot{\Phi}_{s2}-Z_{BP}+\frac{\pi}{2\eta_2}\left(V_{BP2}^{-\frac{\eta_2}{2}}+V_{BP2}^{\frac{\eta_2}{2}}\right)s+\dot{\varphi}_{BP}\right\}$$

where B_{BP1} represents the actual control gain matrix of the IESS. Further, the B_{BP1}, V_{BP2}, s, and φ_{BP} are

$$B_{BP1}=\begin{bmatrix}b_{11}&b_{12}\\b_{21}&b_{22}\end{bmatrix},$$
$$\begin{cases}b_{11}=\frac{k_{\theta1}RTW_{in1}}{t_{\theta1}PV(C_p-R)\theta_1}\left(-(h_{out}-RT)+h_{in1}+\frac{C_{in1}^2}{2}\right),\\ b_{12}=\frac{k_{\theta1}RTW_{in2}}{t_{\theta1}PV(C_p-R)\theta_2}\left(-(h_{out}-RT)+h_{in2}+\frac{C_{in2}^2}{2}\right),\\ b_{21}=\frac{k_{\theta2}RW_{in1}}{t_{\theta2}V\theta_1}\left(T-\frac{h_{out}-RT}{C_p-R}+\frac{1}{C_p-R}\left(h_{in1}+\frac{C_{in1}^2}{2}\right)\right),\\ b_{22}=\frac{k_{\theta2}RW_{in2}}{t_{\theta2}V\theta_2}\left(T-\frac{h_{out}-RT}{C_p-R}+\frac{1}{C_p-R}\left(h_{in2}+\frac{C_{in2}^2}{2}\right)\right),\\ V_{BP2}=\frac{1}{2}s^Ts,\qquad s=e_2+\varphi_{BP},\\ \varphi_{BP}=\frac{\pi}{2\eta\, t_{pd1}}\left(V_{BP1}^{-\eta/2}+V_{BP1}^{\eta/2}\right)e_1,\\ V_{BP1}=\frac{D_p^2}{\pi}\tan\left(\frac{\pi e_1^2}{2D_p^2}\right)+K\frac{D_T^2}{\pi}\tan\left(\frac{\pi e_1^2}{2D_T^2}\right),\\ e_1=Z_{BP1}-\Phi_{s1},\qquad e_2=Z_{BP2}-\Phi_{s2}.\end{cases}$$

(2) MRA-TESO Method

The structure of TESO is

$$\dot{Z}_{MT} = \Gamma_{MT} Z_{MT} + B_{MT} U_{Tp} + L_{MT} Y_M$$

where $Z_{MT} = [Z_{MT1}^T, Z_{MT2}^T, Z_{MT3}^T]^T$ represents the estimation vector of the state of the system. Specifically, $Z_{MT1} = [z_{mt1T}, z_{mt1p}]^T$, $Z_{MT2} = [z_{mt2T}, z_{mt2p}]^T$, and $Z_{MT3} = [z_{mt3T}, z_{mt3p}]^T$ respectively represent the estimates of temperature and pressure, the estimates of differential of temperature and pressure, and the partial disturbances (system model uncertainties, control gain deviations, and rapid flow fluctuations induced by aeroengine thrust transients) of temperature loop and pressure loop. Besides, the Γ_{MT}, L_{MT}, and B_{MT} are presented as:

$$\Gamma_{MT} = \begin{bmatrix} -l_{mt1T} & 0 & 1 & 0 & 0 & 0 \\ 0 & -l_{mt1p} & 0 & 1 & 0 & 0 \\ 0 & 0 & 0 & 0 & 1 & 0 \\ 0 & 0 & 0 & 0 & 0 & 1 \\ -l_{mt3T} & 0 & -l_{mt2T} & 0 & 0 & 0 \\ 0 & -l_{mt3p} & 0 & -l_{mt2p} & 0 & 0 \end{bmatrix}, L_{MT} = \begin{bmatrix} l_{mt1T} & 0 & 0 & 0 \\ 0 & l_{mt1p} & 0 & 0 \\ 0 & 0 & 0 & 0 \\ l_{mt3T} & 0 & l_{mt2T} & 0 \\ 0 & l_{mt3p} & 0 & l_{mt2p} \end{bmatrix},$$

$$B_{MT} = \begin{bmatrix} 0 & 0 \\ 0 & 0 \\ \dfrac{k_{\theta 1} R W_{in1} \left(-(h_{out} - RT) + h_{in1} + \frac{C_{in1}^2}{2} \right)}{t_{\theta 1} P V (C_p - R) \theta_1} & 0 \\ 0 & \dfrac{k_{\theta 2} R W_{in2} \left(T - \frac{h_{out} - RT}{C_p - R} + \frac{h_{in2} + \frac{C_{in2}^2}{2}}{C_p - R} \right)}{t_{\theta 2} V \theta_2} \\ 0 & 0 \\ 0 & 0 \end{bmatrix}.$$

The reference model set as

$$\begin{cases} \dot{X}_{MTr} = A_{MTr} X_{MTr} + B_{MTr} \Phi_{s1} \\ Y_{MTr} = C_{MTr} X_{MTr} \end{cases}$$

where $X_{MTr} = [X_{MTr1}^T, X_{MTr2}^T]^T$ is the state variable vector. Specifically, $X_{MTr1} = [x_{mtr-1Tr}, x_{mtr-1pr}]^T$, $X_{MTr2} = [x_{mtr-2Tr}, x_{mtr-2pr}]^T$. Meanwhile, the forms of A_{mtr}, B_{mtr}, and C_{mtr} as

$$A_{MTr} = \begin{bmatrix} 0 & 0 & 1 & 0 \\ 0 & 0 & 0 & 1 \\ -a_{mt-1Tr} & 0 & -a_{mt-2Tr} & 0 \\ 0 & -a_{mt-1pr} & 0 & -a_{mt-2pr} \end{bmatrix},$$

$$B_{MTr} = \begin{bmatrix} 0 & 0 & b_{mt-1Tr} & 0 \\ 0 & 0 & 0 & b_{mt-1pr} \end{bmatrix}^T, \quad C_{MTr} = \begin{bmatrix} 1 & 0 & 0 & 0 \\ 0 & 1 & 0 & 0 \end{bmatrix}.$$

where the parameters $a_{mt\text{-}1Tr}$, $a_{mt\text{-}2Tr}$, $a_{mt\text{-}1pr}$, $a_{mt\text{-}2pr}$, $b_{mt\text{-}1Tr}$ and $b_{mt\text{-}1pr} \in R^+$.

The corresponding mathematical expression of the control law is as

$$U_{MT} = (B_{MT}^T B_{MT})^{-1} B_{MT}^T \big(\hat{g} \Phi_{s1} + \hat{K}_{MT} [Z_{MT1}^T, Z_{MT2}^T]^T - D_{MT} Z_{MT3} \big) \tag{54}$$

where the D_{MT}, and the adaptive laws for $\hat{g}$ and $\hat{K}_{MT}$ can be derived

$$D_f = \begin{bmatrix} 0 & 0 & 1 & 0 \\ 0 & 0 & 0 & 1 \end{bmatrix}^T,$$

$$\begin{cases} \dot{\hat{g}} = -P_G E_{MTr} X_{MTr1}^T \\ \dot{\hat{K}}_{MT} = -P_K E_{MTr} [Z_{MT1}^T, Z_{MT2}^T] \end{cases}$$

here $E_{MTr} = X_{MTr} - X$. Additionally, $P_G = \mathrm{diag}\{p_{g1T}, p_{g1p}, p_{g2T}, p_{g2p}\}$ and $P_K = \mathrm{diag}\{p_{k1T}, p_{k1p}, p_{k2T}, p_{k2p}\}$.

In particular, the control parameters of the proposed method and the others are summarized in Table 3.

► Analysis of Comparative Results

The experimental results regarding temperature and pressure for the three control methods are depicted in Fig. 7. Notably, it also provides local magnified views of the system responses for a visual assessment of each control method during the system state change. Furthermore, Fig. 8 illustrates the quantitative comparisons using three performance indices: maximum tracking error (MTE), integral of absolute error (IAE=$\int_0^{t_f} |e(t)| dt$, with t_f representing the end time), and reaching time (RT). Obviously, smaller values in terms of MTE, IAE, and RT indicate better control performance.

It is evident from Fig. 7 that all three control methods achieve tracking for both temperature and pressure setpoints in the IESS. However, the proposed method exhibits superior overall control performance compared to the others. Further analysis of Fig. 8 reveals that: 1) compared with BLF-PTDR method, subplots (a) and (b) indicate the proposed method exhibits a marginal improvement in tracking accuracy, whereas subplot (c) demonstrates a prominent advantage in response speed; 2) compared with MRA-TESO method, subplot (c) indicates no substantial improvement in response speed for the proposed method, but subplots (a) and (b) confirm a remarkable enhancement in tracking accuracy. In conclusion, the proposed control method possesses both excellent dynamic tracking performance and rapid system response. Moreover, unlike the two comparative methods that rely on partial information (control gains) of the IESS model, the proposed method exhibits no dependence on it.

Table 3 Parameters of control

Method	Controller	Observer
BLF-PTDR	$\eta = 0.2,\ K = 6 \times 10^5,$ $t_{pd1} = 2,\ t_{pd2} = 1,$ $D_p = 11.5,\ D_T = 0.023$	$l_{bp1T} = l_{bp1p} = 60,$ $l_{bp2T} = l_{bp2p} = 1200,$ $l_{bp3T} = l_{bp3p} = 8000$
MRA-TESO	$a_{mt\text{-}1Tr} = a_{mt\text{-}1pr} = b_{mt\text{-}1Tr} = b_{mt\text{-}1pr} = 2.5,$ $a_{mt\text{-}2Tr} = a_{mt\text{-}2pr} = 5,$ $p_{g1T} = p_{g1p} = p_{g2T} = p_{g2p} = 0.1,$ $p_{k1T} = p_{k1p} = p_{k2T} = p_{k2p} = 0.5$	$l_{mt1T} = l_{mt1p} = 60,$ $l_{mt2T} = l_{mt2p} = 1200,$ $l_{mt3T} = l_{mt3p} = 8000$
Proposed	$b_{0T} = -2,\ b_{0p} = 0.6,$ $a_{1Tr} = a_{1pr} = b_{1Tr} = b_{1pr} = 2.5,\ a_{2Tr} = a_{2pr} = 5,$ $\lambda_{Tx} = \lambda_{px} = 0.01,\ \lambda_{TI} = \lambda_{pI} = 0.05,$ $p = 0.4,\ p_1 = 9,\ p_2 = 2.8$	$l_{m1T} = l_{m1p} = 60,$ $l_{m2T} = l_{m2p} = 1200,$ $l_{m3T} = l_{m3p} = 8000$

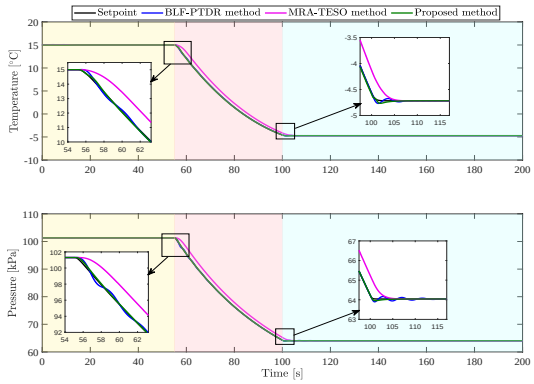


Fig. 7 Comparative experimental results

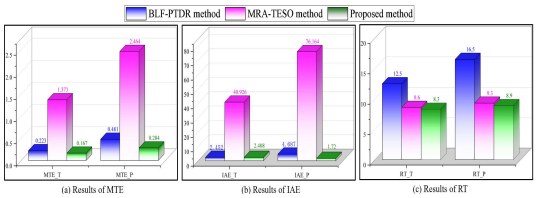


Fig. 8 Visualization of control performance indicators

5.3 Robust Performance

To verify the robustness of the proposed method, experiments are carried out from two aspects in this section: on the one hand, based on transient environment simulation task to examine its disturbance rejection capability; on the other hand, based on continuous flight trajectory environment simulation task to evaluate its ability to maintain control performance in response to rapid change in flight commands.

► Transient Environment Simulation

Under the takeoff process environment simulation task, a throttle lever swing function is imposed during the 130 $\sim$ 150 s interval to represent the disturbances caused by drastic fluctuations in the aeroengine air mass flow rate. About the function, a linear ramp-up from 10° to 48° is executed from 130 to 135 s, a constant state at 48° is maintained from 135 to 145 s, and a linear decrease back to 10° is subsequently implemented from 145 to 150 s, by which the transient dynamic changes in the aeroengine operating state are simulated. At the same time, a random noise function with an amplitude of 0.01 is applied to represent the inter-loop crosstalk during the period from 170 to 175 s. The corresponding results are presented in Fig. 9. It can be observed that slight deviations occur in the tracking of both temperature and pressure setpoint signals. To quantitatively evaluate the disturbance rejection performance of the proposed method, Fig. 10 presents the MTE and IAE over a continuous 55 s analysis interval composed of the 130 $\sim$ 185 s period. The result demonstrates that the proposed method not only enables temperature and pressure fluctuations to rapidly converge to the setpoints, but also exhibits superior disturbance rejection capability compared to the others.

► Continuous Flight Trajectory Environment Simulation

The continuous flight trajectory environment simulation task encompasses multiple consecutive flight phases (as shown in Table 4). To intuitively present the simulation procedure, Fig. 11 employs a light-to-dark color gradient to visualize

Table 4 Continuous flight trajectory environment simulation procedure

Phase	Time (s)	Mach number variation (Ma)	Altitude variation (Km)	Interpretation
1	0∼55	0∼0	0∼0	Ground taxi
2	55∼100	0∼0.5	0∼5	Accelerated ascent
3	100∼110	0.5∼0.5	5∼5	Cruise
4	110∼130	0.5∼0.9	5∼11	Accelerated ascent
5	130∼140	0.9∼0.9	11∼11	Cruise
6	140∼160	0.9∼0.9	11∼8	Uniform descent
7	160∼170	0.9∼0.9	8∼8	Cruise
8	170∼210	0.9∼0	8∼0	Decelerated landing
9	210∼250	0∼0	0∼0	Ground taxi

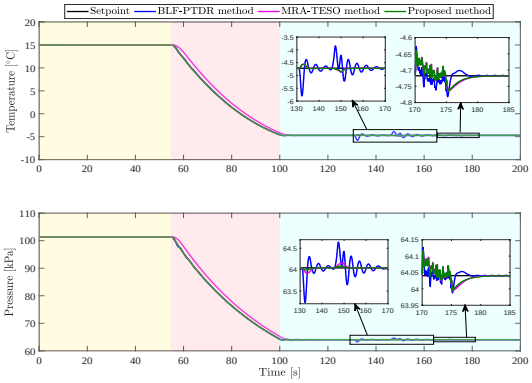


Fig. 9 Results with transient environment simulation

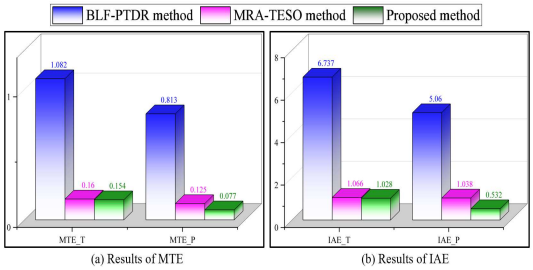


Fig. 10 Control performance indicators within the range of 130 ∼ 185 s

the evolution across different phases. Next, with the parameters in Eqs.(50), (52), and Table 3 kept unchanged, we apply both the proposed method and the comparative methods to the simulation, with the results presented in Fig. 12. As observed from Figs. 12 and 13, the proposed control method continues to achieve temperature and pressure tracking in the IESS with faster response speeds and higher accuracy. To summarize, the proposed control method achieves continuous and accurate tracking of temperature and pressure in the IESS, demonstrating a broader range of applicability. In conclusion, the method exhibits excellent robustness when handling continuous trajectory environment simulation tasks composed of multiple flight phases.

6 Conclusions

Focusing on aeroengine high-altitude environmental simulation testing, this paper presents a TMRA-MATESO-based method for high-precision tracking and robust disturbance rejection. The proposed method enables real-time control of the IESS temperature and pressure while effectively mitigating drastic oscillations induced by disturbances, thereby substantially improving the overall safety and reliability of the test. In particular, the mathematical model of the IESS is reconstructed by separating total disturbances of system into internal and external components, establishing a disturbance-separation-based estimation and control framework. Subsequently, a MATESO incorporating transformation variables

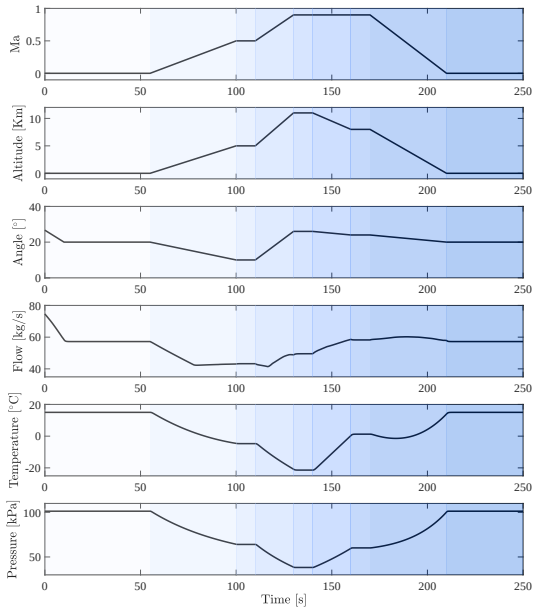


Fig. 11 Continuous flight trajectory environment simulation task

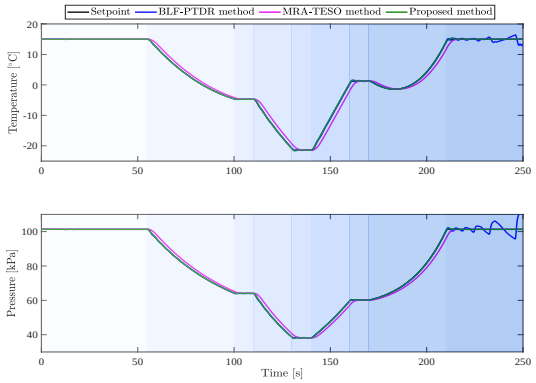
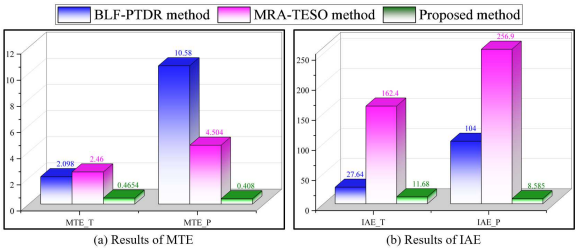


Fig. 12 Results with continuous flight trajectory environment simulation



(a) Results of MTE (b) Results of IAE

Fig. 13 Control performance indicators under continuous flight trajectory environment simulation

and system state variables parameters is designed, and a TRM integrated with adaptive mechanisms is developed. Through deep coupling mechanisms, the system significantly enhances disturbance estimation and compensation, thereby achieving precise temperature and pressure tracking. By using the Lyapunov lemma and LaSalle's invariance theorem, the asymptotic stability of the closed-loop system is rigorously proved. A series of experimental results and data analysis confirm that the proposed method not only exhibits excellent rapid response and high-precision tracking characteristics but also demonstrates superior robustness in the face of complex disturbances.

However, the proposed method does not yet take into account the safety constraints for valve operation presented in Eq.(2), including the boundary limits on valve opening and its rate of change, and it also does not address the cooperative control mechanism between dual valves. Given that these factors exert a significant impact on the reliability and efficient operation of the IESS under actual working conditions, subsequent research will be dedicated to an in-depth exploration of these challenges.

Acknowledgements. This work was supported in part by the National Natural Science Foundation of China under Grant 62003088 and in part by the Foundation Strengthening Priority Project under Grant JWKT-2001-2022-0002.

Author contributions. X. Xu conceived the proposed method, wrote the main manuscript, and prepared Figs. 1–13 and Tables 1–4. H. Zhang acquired the funding and designed the study. X. Wang performed the experiments and analyzed the data. C. Zhai, C. Zhang, and B. Zhang contributed to the theoretical analysis and method design. F. Huang reviewed and edited the manuscript. All authors read and approved the final manuscript. X. Xu, F. Huang, X. Wang, C. Zhai, C. Zhang, B. Zhang, and H. Zhang contributed equally to this work.

Funding. National Natural Science Foundation of China (62003088) and Foundation Strengthening Priority Project (JWKT-2001-2022-0002).

Data Availability. The datasets generated and analysed during the current study are not publicly available due to the proprietary nature of the

test-rig configuration, but are available from the corresponding author on reasonable request.

Statements and Declarations

Conflict of interest. The authors declare no competing interests.

References

[1] Chao, L., Guo, H., Xu, Y., He, Y., Liang, G.: Green run test assessment of the high-altitude simulation test facility for liquid attitude and orbit control engines. Aerosp. Sci. Technol. **168**, 110862 (2025) https://doi.org/10.1016/j.ast.2025.110862

[2] Xu, Z., Zhang, H., Xie, Y., Wang, X., Zhai, C.: Active disturbance rejection control for flight test chamber system subject to multi-source disturbances: An extended state observer with dynamic compensation approach. Aerosp. Sci. Technol. **176**, 112123 (2026) https://doi.org/10.1016/j.ast.2026.112123

[3] Pei, X., Wang, X., Liu, J., Zhu, M., Dan, Z., He, A., Miao, K., Xu, Z.: A review of modeling, simulation, and control technologies of altitude ground test facilities for control application. Chin. J. Aeronaut **36**(9), 38–62 (2023) https://doi.org/10.1016/j.cja.2023.07.014

[4] Davis, M., Montgomery, P.: A flight simulation vision for aeropropulsion altitude ground test facilities. J. Eng. Gas Turbines Power **127**(1), 8–17 (2005) https://doi.org/10.1115/1.1806452

[5] Zou, Z., Zhou, X., Huang, J., Jiang, W., Lu, F.: An online gas path fault diagnosis for aircraft engine transient behavior using ib-ekf algorithm. IEEE Trans. Aerosp. Electron. Syst. **61**(2), 2659–2678 (2024) https://doi.org/10.1109/taes.2024.3478190

[6] Zhang, H., Xie, Y., Wang, J., Dan, Z., Guo, W.: Parameter tuning algorithm for levant's differentiator and its application in flight environment simulation control system. Control Theory Appl. **40**(10), 1831–1838 (2023) https://doi.org/10.7641/CTA.2022.10361

[7] Han, J.: From pid to active disturbance rejection control. IEEE Trans. Ind. Electron. **56**(3), 900–906 (2009) https://doi.org/10.1109/tie.2008.2011621

[8] Gao, Z.: Scaling and bandwidth-parameterization based controller tuning. Proc. Amer. Control Conf. **4**(2), 4989–4996 (2003) https://doi.org/10.1109/acc.2003.1242516

[9] Zhuang, X., Guo, Y., Tian, Y., Wang, H.: A sampled delayed output extended state observer-based adaptive feedback control of robot manipulator with unknown dynamics. Nonlinear Dyn. **111**(24), 22283–22301 (2023) https://doi.org/10.1007/s11071-023-09022-4

[10] Cao, Y., Yang, W., Wang, S., He, S., Liu, Z., Xie, L.: Improved trajectory tracking control for a continuum robot using error-driven adrc with input mapping method. IEEE Trans. Ind. Electron. **71**(10), 12696–12706 (2024) https://doi.org/10.1109/tie.2023.3344834

[11] Li, R., Li, M., Qiu, J., Li, K., Liu, Y., Cui, C., Fu, S., Ma, B., Zhang, Q., Cui, M.: Precise robotic picking up of polar body for biopsy application. IEEE Trans. Autom. Sci. Eng. **22**, 5895–5905 (2024) https://doi.org/10.1109/tase.2024.3432572

[12] Guo, J., Lu, R., Yao, D., Zhou, Q.: Implementation of the load frequency control by two approaches: variable gain super-twisting algorithm and super-twisting-like algorithm. Nonlinear Dyn. **93**(3), 1073–1086 (2018) https://doi.org/10.1007/s11071-018-4246-6

[13] Li, M., Fei, J.: Self-structured chebyshev fuzzy neural sliding mode control with linear extended state observer for active power filter. Nonlinear Dyn. **113**(24), 33563–33585 (2025) https://doi.org/10.1007/s11071-025-11732-w

[14] Lu, H., Li, J., Li, S., Wang, S., Xiao,

Y.: Finite-time extended state observer enhanced nonsingular terminal sliding mode control for buck converters in the presence of disturbances: design, analysis and experiments. Nonlinear Dyn. **112**(9), 7113–7127 (2024) https://doi.org/10.1007/s11071-024-09381-6

[15] Gu, S., Liu, S., Yan, M., Zhao, D.: Generalized finite-time variable gain composite adrc for nonlinear systems and its application to vehicle active suspensions. IEEE Trans. Ind. Electron. **73**(6), 9116–9127 (2026) https://doi.org/10.1109/tie.2025.3647879

[16] Lv, H., Wang, X., Xie, B., Shi, B., Li, Q., Xu, Y., Cheng, L.: A hierarchical cooperative control strategy for in situ steering of distributed drive electric vehicle. IEEE Trans. Transp. Electrif. **11**(3), 8427–8438 (2025) https://doi.org/10.1109/tte.2025.3540866

[17] Wang, Y., Dong, L., Chen, Z., Sun, M., Long, X.: Integrated skyhook vibration reduction control with active disturbance rejection decoupling for automotive semi-active suspension systems. Nonlinear Dyn. **112**(8), 6215–6230 (2024) https://doi.org/10.1007/s11071-024-09337-w

[18] Hou, Y., Li, X., Wang, S.: An adaptive composite anti-disturbance control for slung payload stabilization of an unmanned tandem helicopter. Aerosp. Sci. Technol. **168**, 110971 (2025) https://doi.org/10.1016/j.ast.2025.110971

[19] Wang, Z., Zhao, T.: Based on robust sliding mode and linear active disturbance rejection control for attitude of quadrotor load uav. Nonlinear Dyn. **108**(4), 3485–3503 (2022) https://doi.org/10.1007/s11071-022-07349-y

[20] Hua, C.-C., Wang, K., Chen, J.-N., You, X.: Tracking differentiator and extended state observer-based nonsingular fast terminal sliding mode attitude control for a quadrotor. Nonlinear Dyn. **94**(1), 343–354 (2018) https://doi.org/10.1007/s11071-018-4362-3

[21] Xu, Z., Zhang, H., Zhai, C., Xiao, G., Qian, Q., Huang, F.: Active disturbance rejection intake pressure control of aeropropulsion systems test facility with adaptive parameter b_0. Aerosp. Sci. Technol. **163**, 110289 (2025) https://doi.org/10.1016/j.ast.2025.110289

[22] Li, C., Zhang, H., Xie, Y., Huang, F., Wang, X.: Design and implementation of a dual-core third order time-optimal tracking differentiator in the flight environment simulation system. Aerosp. Sci. Technol. **168**, 111176 (2025) https://doi.org/10.1016/j.ast.2025.111176

[23] Li, C., Zhang, H., Xiao, G., Zhai, C., Dan, Z., Wang, X.: An efficient tracking differentiator based active disturbance rejection control for flight environment simulation system. Aerosp. Sci. Technol. **155**, 109578 (2024) https://doi.org/10.1016/j.ast.2024.109578

[24] Zheng, B., Zhang, H., Wang, X., Zhai, C., Lin, H., Li, X.: Eso-mpc and differential flatness-based multivariable control of high-altitude chamber intake systems. J. Aerosp. Eng. **39**(3), 04026010 (2026) https://doi.org/10.1061/jaeeez.aseng-6702

[25] Li, J., Lun, Y., Wang, H., Qian, Q., Zhang, S., Dan, Z.: A predefined-time disturbance rejection control for multitasking simulation of altitude test facilit. J. Propuls. Technol. **45**(9), 241–251 (2024) https://doi.org/10.13675/j.cnki.tjjs.2308039

[26] Jin, Y., Cui, P., Zhang, H., Li, Y., Yang, Z.: Mra-teso based high-precision active magnetic compensation method. IEEE Trans. Autom. Sci. Eng. **22**, 19095–19105 (2025) https://doi.org/10.1109/tase.2025.3592993

[27] Zhu, M., Wang, X., Pei, X., Dan, Z., Gu, N., Yang, S., Miao, K., Chen, H., Liu, J.: Modified robust optimal adaptive control for flight environment simulation system with heat transfer uncertainty. Chin. J. Aeronaut **34**(2), 420–431 (2021) https://doi.org/10.1016/j.cja.2020.03.017

[28] Liu, J., Wang, X., Liu, X., Pei, X., Dan, Z., Zhang, S., Yang, S., Zhang, L.: An anti-windup design with local sector and H_2/H_∞

optimization for flight environment simulation system. Aerosp. Sci. Technol. **128**, 107787 (2022) https://doi.org/10.1016/j.ast.2022.107787

[29] Lee, S., Kim, J.J., Kim, D., Kim, K., Cho, J., Shin, W.: Novel far-end crosstalk noise canceling structure with floating shape in memory module. IEEE Trans. Signal Power Integr. **4**, 136–140 (2025) https://doi.org/10.1109/tsipi.2025.3568775

[30] Khalil, H.: Nonlinear systems. 3rd ed. englewood cliffs, nj: Prentice-hall (2002)

[31] Zhu, M., Wang, X., Dan, Z., Pei, X.: Two freedom linear parameter varying μ synthesis control for flight environment testbed. Chin. J. Aeronaut **32**(5), 1204–1214 (2019) https://doi.org/10.1016/j.cja.2019.01.017